Article

Investigation of the Structural Heterogeneity and Corrosion Performance of the Annealed Fe-Based Metallic Glasses

Dandan Liang [1,2], Jo-Chi Tseng [1], Xiaodi Liu [1], Yuanfei Cai [3], Gang Xu [1] and Jun Shen [1,*]

[1] College of Mechatronics and Control Engineering, Shenzhen University, Shenzhen 518060, China; liangdandanup@szu.edu.cn (D.L.); jochi.tseng@szu.edu.cn (J.-C.T.); xdliu2018@szu.edu.cn (X.L.); xugang@szu.edu.cn (G.X.)
[2] Key Laboratory of Optoelectronic Devices and Systems of Ministry of Education and Guangdong Province, College of Optoelectronic Engineering, Shenzhen University, Shenzhen 518060, China
[3] College of Materials Science and Engineering, Tongji University, Shanghai 201804, China; yzcaiyuanfei@tongji.edu.cn
[*] Correspondence: junshen@szu.edu.cn; Tel.: +86-755-2653-4231

Abstract: This study investigated the structural heterogeneity, mechanical property, electrochemical behavior, and passive film characteristics of Fe–Cr–Mo–W–C–B–Y metallic glasses (MGs), which were modified through annealing at different temperatures. Results showed that annealing MGs below the glass transition temperature enhanced corrosion resistance in HCl solution owing to a highly protective passive film formed, originating from the decreased free volume and the shrinkage of the first coordination shell, which was found by pair distribution function analysis. In contrast, the enlarged first coordination shell and nanoscale crystal-like clusters were identified for MGs annealed in the supercooled liquid region, which led to a destabilized passive film and thereby deteriorated corrosion resistance. This finding reveals the crucial role of structural heterogeneity in tuning the corrosion performance of MGs.

Keywords: metallic glass; synchrotron radiation; heterogeneity; electrochemical behavior; passive film

1. Introduction

Due to the homogenous amorphous structure (no grain boundaries, inclusions, or precipitates), metallic glasses (MGs) exhibit superior strength and hardness, excellent corrosion resistance, low cost, etc. [1,2]. However, with the continuous exploration of amorphous structure, the homogenous microstructure of MGs is found out to be heterogeneous at the nanoscale or microscale. For instance, Hirata et al. proved the local atomic order in metallic glasses by nanobeam electron diffraction combined with ab initio molecular dynamics simulation [3] and then revealed the relation between the nanoscale spatial heterogeneity and the local structure variation from icosahedron-like to tetragonal crystal-like order in MGs [4]. Wagner and Liu et al. characterized the inhomogeneous distribution of local elastic modulus and energy dissipation utilizing atomic force microscopy (AFM) [5,6], which quantified the structural heterogeneity in MGs. The high-energy X-ray or neutron diffraction could detect the spatial heterogeneity in MGs from atomic-scale to nanoscale without destroying the sample [7,8].

Recently, understanding the structural heterogeneity of MGs and its relation to the intrinsic properties is an area of interest for researchers [9]. Intensive studies focused on the relationships between the structural heterogeneity of MGs and superplasticity [10,11], thermal expansion [12], magnetoelastic effect [13], catalytic performance for dye degradation [14], electrochemical supercapacitors [15], and hydrogen generation [16]. Nevertheless, the correlation between structural heterogeneity and corrosion is still an open topic. On the one hand, the decreased free volume promotes the formation of a highly protective passive film and enhances the corrosion resistance of the relaxed MGs [17,18]. Tailleart et al. [19]

reported that the structural relaxation favors the solute enrichment and passivation because it eliminates free volume and annihilates vacancies. The nanoscale elemental partitioning of MGs determines the degree of passivation [20]. On the other hand, Jindal and co-workers [21] unveiled that the structural changes are irrelevant with the improved passivity of the relaxed MGs. Moreover, the structural relaxation reduces the atomic mobility of strong passivating elements in MGs and further inhibits the formation of passive films [22]. Thus, the correlation between the structural heterogeneity and corrosion performance remains to be understood.

In this study, $Fe_{43}Cr_{20}Mo_{10}W_4C_{15}B_6Y_2$ (at %) glassy ribbons with high glass-forming ability (GFA) and excellent corrosion resistance were examined. The structural heterogeneity, electrochemical behavior, and passive film characteristics of MGs were modified through isothermal annealing at different temperatures. The effect of annealing on the structural heterogeneity of Fe-based MGs was realized from a microscale perspective via a combination of synchrotron radiation (SR) X-ray total scattering and high-resolution transmission electron microscopy (HRTEM) techniques. In addition, the correlation between structural heterogeneity and corrosion performance of MGs was also discussed.

2. Materials and Methods

2.1. Preparation and Characterization of MGs

Master ingots with a nominal composition of $Fe_{43}Cr_{20}Mo_{10}W_4C_{15}B_6Y_2$ (at %) were prepared by arc melting a mixture of commercial-purity Fe (99.95 wt %), Cr (99.95 wt %), Mo (99.95 wt %), W (99.95 wt %), Y (99.9 wt %), C (99.95 wt %), and B (99.9 wt %) in Ti-gettered Ar atmosphere. Approximately 40 μm thick and 1.2 mm wide metallic glasses (MGs) were produced using a single-wheel melt-spinning technique in Ar atmosphere with a wheel speed of 35 m/s.

The thermal stability of the melt ribbons was determined by a differential scanning calorimeter (DSC, Netzsch 404C, Waldkraiburg, Germany) with a heating rate of 20 K/min. Based on the DSC responses in Figure 1b, the glass transition temperature (T_g) and the onset of crystallization temperature (T_x) of the initial A0 samples were measured to be approximately 858 and 920 K, respectively. Afterward, A0 samples were heated to 0.7 T_g and T_g + 10 K for 30 min under Ar flow to obtain two independent A1 and A2 samples, respectively. Phase characterization of MGs was carried out by utilizing an X-ray diffractometer (XRD, Rigaku MiniFlex600, Austin, TX, USA) accompanied with Cu K_α radiation.
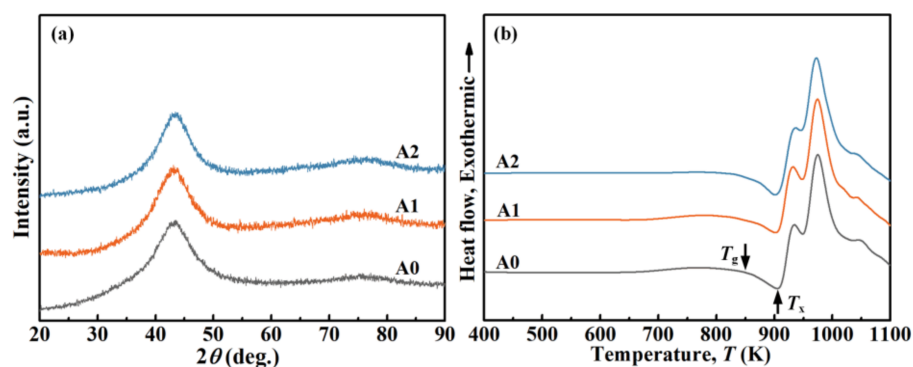

Figure 1. (**a**) X-ray diffractometer (XRD) patterns and (**b**) differential scanning calorimeter (DSC) curves of the initial and annealed Fe-based MGs.

To exploit the structural heterogeneity of Fe-based MGs, the total scattering experiments were conducted at Beamline P02.1, DESY (PETRA III), where the high-energy X-ray of about 60 keV (wavelength ≈0.207 Å) was beneficial for a large scattering vector (q) range collection. Each measurement was collected with 30 s detection, and the Perkin-Elmer EN1621 2D detector (Hamburg, Germany) was used. The sample-to-detector distance was set to 243 mm, and the q_{max} of the total scattering data reached 24 Å^{-1}. The raw

2D scattering data were integrated by DAWN [23,24]. Subsequently, the pair distribution function (PDF) was obtained using the software package PDFgetX2 to understand the local structure of the samples [25]. The q range was limited to 1–20 Å^{-1} in the Fourier transform because of low statistics at high scattering angles. Furthermore, the microstructure was observed via a transmission electron microscope (TEM, JEM F200, Akijima, Tokyo, Japan) with an operating voltage of 200 kV. TEM foils were prepared using a focused ion beam (FIB, FEI Scios, Hillsboro, OR, USA), and the specific FIB parameters were clarified in our previous work [26].

2.2. Nanoindentation Tests

The mechanical property of MGs was investigated by nanoindentation tests utilizing a triboindenter (Hysitron TI-950, Eden Prairie, MN, USA). Prior to testing, the triboindentater was calibrated with fused quartz. Nanoindentation experiments were performed in a load-control mode using a diamond Berkovich indenter. The constant loading and unloading rates were 1600 µN/s, the maximum applied load was 8000 µN, and the holding time at maximum load was 2 s in all cases. Each indentation test was repeated nine times to ensure the acceptable reliability of the data collected.

2.3. Electrochemical Measurements

Electrochemical measurements were performed with a three-electrode electrochemical workstation (Gamry Reference 60+) with a platinum sheet as the counter electrode, a saturated calomel electrode (SCE) as the reference electrode, and the samples as the working electrode. First, 1 mol/L HCl solution was selected as the electrolyte. Prior to the electrochemical tests, all samples were mechanically ground with 2000-grit metallographic sandpaper, cleaned with ethanol, and dried. Once the open circuit potential (OCP) was stabilized after immersing in the electrolyte for 30 min, electrochemical impedance spectroscopy (EIS) tests were conducted at the OCP with a sinusoidal amplitude of 10 mV and a frequency range of 10^5–10^{-2} Hz. The EIS outcomes were fitted on the basis of the equivalent electrical circuit via ZSimpWin software (Version 3.30d, AMETEK Scientific Instruments, Michigan, USA). The potentiodynamic polarization was executed from -0.3 V_{OCP} to $+1.2$ V_{SCE} with a sweep rate of 0.5 mV/s. The samples were independently polarized at 0.5 V_{SCE} for 30 min in 1 mol/L HCl solution to obtain stable passive films. Afterward, the Mott–Schottky measurements of the formed passive films were conducted from 0 to 1.0 V_{SCE} with a measurement frequency of 10^3 Hz and a scan rate of 10 mV/s. All electrochemical measurements were performed at room temperature and repeated thrice to guarantee data reliability.

2.4. XPS Analysis

The depth profiles of the passive films that formed on the surface of MG samples were examined through X-ray photoelectron spectroscopy (XPS, ESCALAB250Xi, Waltham, MA, USA) with a monochromated Al K_{α} X-ray source ($h\nu$ = 1486.6 eV) and a controlled Ar-ion beam sputtering rate of 0.05 nm/s. The binding energy was calibrated by setting the Au $4f_{7/2}$ peak of pure Au sample at a binding energy of 83.96 ± 0.02 eV. XPS responses were analyzed via CasaXPS software (Version 2.3.16, Los Angeles, CA, USA). Prior to the tests, all samples were ultrasonically cleaned with alcohol to eliminate any surface impurities.

3. Results and Discussion

3.1. Characteristics of Fe-Based MGs

The XRD patterns of the initial and annealed MG samples in Figure 1a show a similar configuration, namely, a broad halo peak around 2θ range of 40–50° without any crystalline diffraction peak, indicating their amorphous traits within the XRD resolution [27]. Moreover, all DSC thermograms in Figure 1b exhibit a wide supercooled region ΔT_x ($T_x - T_g$) followed by three exothermic crystallization events. As shown in Figure 1b, the exothermic heat that occurs below T_g, that is, the structural relaxation exothermic heat (ΔH_{rel})

decreases from ≈7.51 J/g for the A0 sample to ≈6.71 J/g for the A1 sample and ≈0 J/g for the A2 sample, respectively. It is noteworthy that the difference in ΔH_{rel} is proportional to the amount of annihilated free volume during the isothermal annealing process [28–30]. Therefore, the decreased ΔH_{rel} corresponds to the release of free volume in the amorphous structure, especially the elimination of most of the free volume in the A2 MG. Moreover, the crystallization enthalpy (ΔH_{cry}) of A0, A1, and A2 samples, namely, the integrity of crystallization peaks above T_g [31], are measured to be ≈87.50, ≈87.84, and ≈76.56 J/g, respectively. Compared to the original A0 sample, the nearly same ΔH_{cry} of A1 sample suggests the unoccurring crystallization during annealing below T_g, whilst the slightly reduced ΔH_{cry} of A2 sample indicates the sporadic crystallization during annealing in the supercooled liquid region. From the perspective of potential energy landscape (PEL), many local potential energy minima (also called inherent structures or ISs) exist in amorphous materials, and they represent the metastable states [32–34]. Annealing below T_g induces hopping between contiguous ISs, thus modifying the glassy structure with different degrees of disorder in A1 MG [35]. However, annealing MG in the supercooled liquid region can reduce the energy barrier between the glassy phase and crystalline phase, resulting in the heterogeneous nucleation sites in A2 MG [36]. Whereafter, high-resolution characterizations were taken to further understand the effect of annealing on the structural heterogeneity of MGs.

SR X-ray total scattering experiments were performed to exploit the local atomic structure information of Fe-based MGs. PDF analysis is used to calculate $G(r)$, which is a pair correlation that represents the probability of finding atoms as a function of distance r from an average center atom [37]. In Figure 2, all $G(r)$ patterns show strong oscillation spanning from 2 to 16 Å, reflecting the existence of short-range order (SRO) and medium-range order (MRO) in the atomic arrangement of all tested samples. The fluctuating pattern and the splitting of the second peaks reveal the typical amorphous traits [38]. The radius of the first coordination shell, given in r_1, of the initial A0 and annealed A1 samples are determined to be 2.65 and 2.63 Å, respectively. An opposite observation is shown for the annealed A2 sample. The shift of r_1 from 2.65 to 2.67 Å indicates a larger first coordination shell and lower atomic packing density in the local structure of A2 sample. The enhanced intensities of the r_3 and r_4 peaks signify the increased amount of MROs for MGs annealed in the supercooled liquid region.
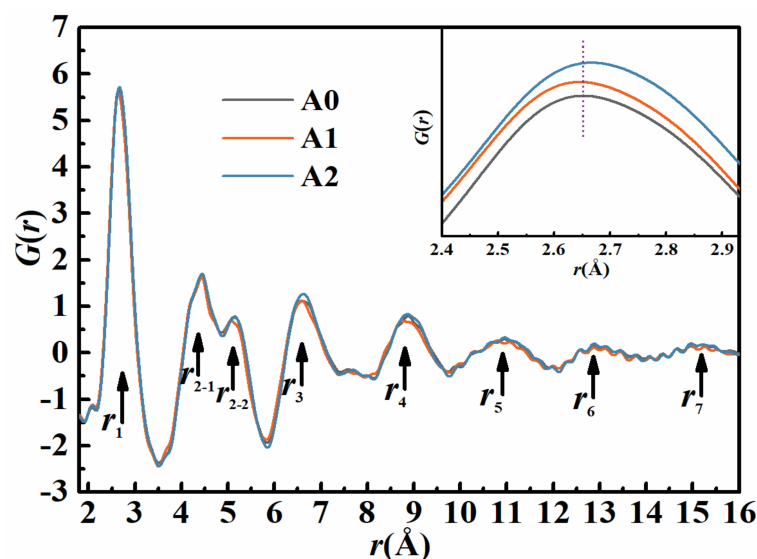

Figure 2. Pair distribution functions of Fe-based metallic glasses (MGs).

To give a solid vision in the structure–property relationship, not only the PDF analysis giving as averaging information but also the HRTEM and the selected area electron diffraction (SAED) were applied to characterize locally atomic-scale structure changes in MGs. As

shown in Figure 3a–c, the bright halos in the SAED patterns demonstrate the amorphous structure in all three samples. The HRTEM image of A0 sample in Figure 3a depicts a maze configuration without any crystalline fringes. The existence of abundant icosahedron-like SROs with five-fold symmetry is the structural origin of its superior GFA [39]. For the A1 sample, annealing at 0.7 T_g assists the release of free volume, the elimination of "liquid-like" regions, and the generation of numerous "solid-like" regions in the amorphous structure [40]. As a result, the atomic arrangement of A1 MG is more compact, which is in accordance with DSC and PDF analysis. However, for MG annealed at T_g + 10 K, namely the A2 sample, several nanoscale crystal-like clusters with an ordered atomic arrangement are observed (Figure 3c). Local straight lattice fringes are illustrated in the inverse fast Fourier Transform (IFFT) pattern of Region I, as depicted in Figure 3d. In addition, the enhanced intensities of r_3 and r_4 peaks in G(r) pattern illustrate the increased amount of MROs, which correspond to the nanoscale crystal-like clusters in the HRTEM image for A2 MG. These crystal-like clusters can be regarded as nuclei seeds and trigger an "avalanche-like nucleation" during the further crystallization of MGs [39]. However, the SAED pattern in Figure 3c only exhibits one bright halo without diffraction spots, which is probably because the content and size of crystal-like clusters in the A2 sample are too small, as indicated by the DSC, PDF, and TEM results. It is noteworthy that these distinct microstructures in three samples are considered as the crucial factors in tuning the mechanical and corrosion properties of MGs.
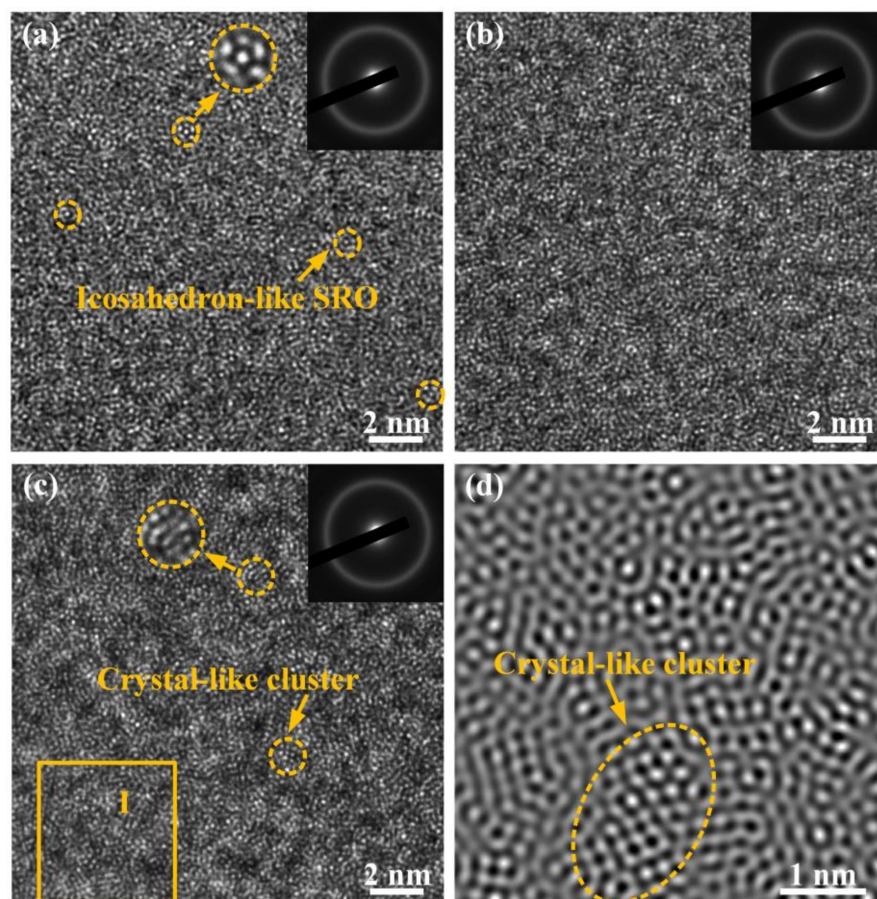

Figure 3. HRTEM images and selected area electron diffraction (SAED) patterns of (**a**) the initial and annealed MGs at (**b**) 0.7 T_g and (**c**) T_g + 10 K, and (**d**) inverse fast Fourier Transform (IFFT) pattern of Region I.

3.2. Mechanical Property of Fe-Based MGs

The typical nanoindentation load–displacement curves of Fe-based MGs are presented in Figure 4a. Under the same load and loading rate, the variation of the maximum contact

depth is in the following tendency: A2 > A0 > A1, indicating the hardest characteristic of A1 MG. Furthermore, the variation of the slope of the unloading segments shows the opposite tendency, which suggests the highest stiffness of A1 MG. The specific reduced elastic modulus (E_r) and nano-hardness (H_n) can be calculated on the basis of the Oliver and Pharr method [41]. For the A0 sample, E_r is 185.72 GPa and H_n is 13.75 GPa. As expected, E_r and H_n of the A1 sample increase to 210.72 and 14.45 GPa, respectively. The increase in modulus usually indicates a decrease in the atomic distance [42]. As indicated by the aforementioned analyses, the released free volume in A1 MG results in a more compact atomic arrangement and thereby a higher E_r. The initiation of shear bands is supposed to be more difficult in local sites with less free volume. Thus, the sequential shear bands in A1 MG require higher stresses to form, which leads to higher hardness [43]. Interestingly, after annealing MG above T_g, E_r and H_n of the A2 sample decrease to 160.24 and 13.61 GPa, respectively. This phenomenon can be explained by the enlarged atomic distance in local sites and the precipitation of nanoscale crystal-like clusters in A2 MG, as shown in Figures 2 and 3. These medium-range ordering (MRO) clusters disturb the relatively disordered atomic arrangement [44,45] and might bring about the enlarged atomic distance in local sites, thereby reducing the modulus and hardness of A2 MG. Therefore, the variation in modulus is highly consistent with the PDF analysis.
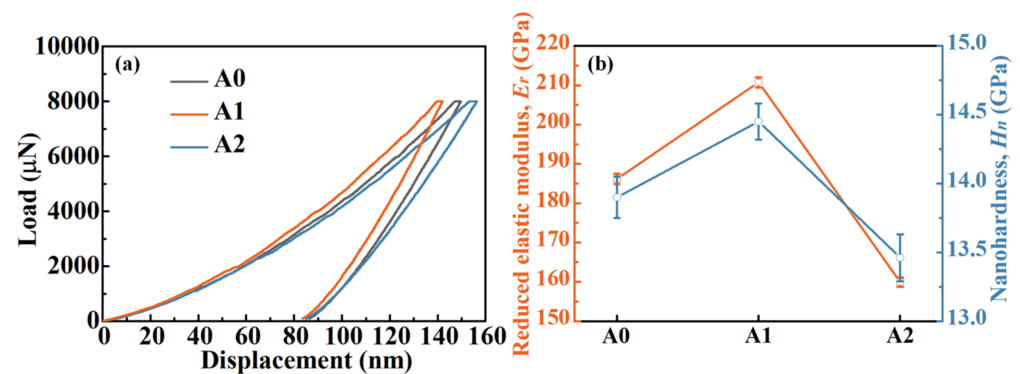

Figure 4. (**a**) Nanoindentation load–displacement plots and (**b**) the calculated E_r and H_n of Fe-based MGs.

3.3. Electrochemical Measurements of MGs

All potentiodynamic polarization curves in Figure 5a show a wide current density plateau and a highly positive passive–active transition potential, which indicates the superior passivity and pitting resistance of MGs. As a result of the high chemical stability of Cr-, Mo-, and W-oxides in HCl solution, a passive barrier film could be spontaneously formed, resulting in a low passive current density (i_{pass}) with a magnitude of 10^{-5}–10^{-6} A/cm^{-2}. Moreover, all Nyquist plots in Figure 5b depict only one capacitive loop, which implies the single time-constant representation of the impedance behavior at the electrode/solution (E/S) interface [46]. The equivalent electrical circuit in Figure 6 matches well with the EIS spectra. Herein, R_s, R_c, and CPE_{dl} represent the solution resistance, charge transfer resistance, and deviation from a non-ideal capacitor, respectively. The calculated electrochemical parameters are summarized in Table 1. For the A1 sample, the lowest i_{pass} and highest pitting potential E_{pit}, which are 4.62 µA/cm^2 and 938.87 mV, respectively, indicate that the passive film formed on the surface of the A1 sample displays the best barrier characteristic among all others. Contrary to the A1 sample, the highest i_{pass} (13.67 µA/cm^2) and the lowest E_{pit} (886.00 mV) are detected for the A2 sample, revealing the weakened protectiveness of the passive film formed on its surface. Moreover, the fitted R_c values of the A0, A1, and A2 samples are 300.32, 458.75, and 202.46 kΩ·cm^2, respectively. High R_c refers to superior passive film stability and excellent corrosion resistance [47]. Hence, the fitted EIS outcomes are highly consistent with the potentiodynamic polarization results. In brief, annealing MG at 0.7 T_g leads to a decreased i_{pass}, elevated R_c, and increased E_{pit}, indicating the enhanced corrosion resistance. Whereas, annealing MG at T_g + 10 K

results in an increased i_{pass}, declined R_c, and decreased E_{pit}, suggesting the deteriorated corrosion resistance.
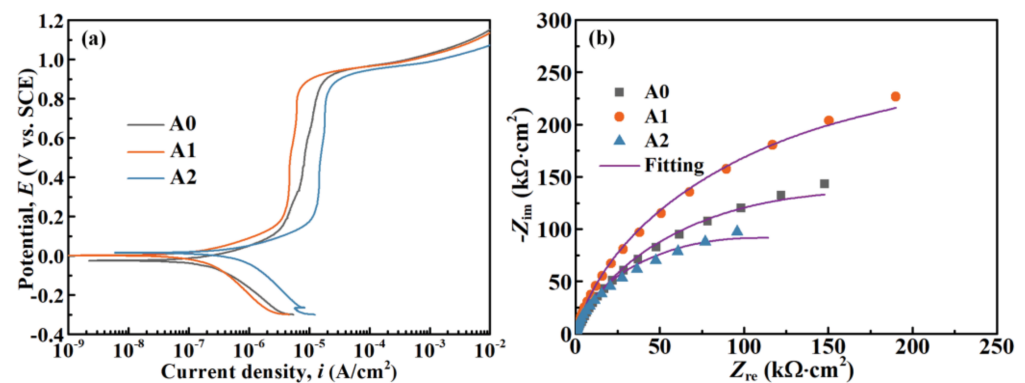

Figure 5. (**a**) Potentiodynamic polarization and (**b**) Nyquist curves of the initial and annealed Fe-based MGs.
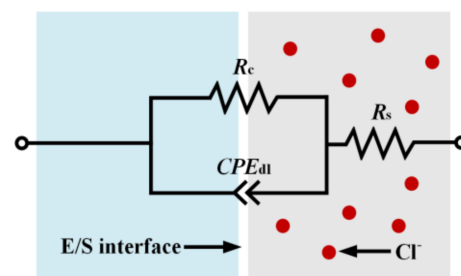

Figure 6. Equivalent electrical circuit model utilized to simulate the electrochemical impedance spectroscopy (EIS) spectra. Electrode/solution (E/S) interface represents the electrode–solution interface.

Table 1. Electrochemical parameters of the initial and annealed Fe-based MGs.

Sample	i_{corr} (µA/cm^2)	E_{corr} (mV)	i_{pass} (µA/cm^2)	E_{pit} (mV)	R_c (kΩ·cm^2)
A0	0.21 ± 0.12	-25.64 ± 17.62	8.45 ± 0.31	923.01 ± 3.32	300.32 ± 12.74
A1	0.34 ± 0.15	-1.82 ± 2.56	4.62 ± 0.73	938.87 ± 0.16	458.75 ± 14.78
A2	0.54 ± 0.11	30.62 ± 14.57	13.67 ± 2.94	886.00 ± 15.24	202.46 ± 10.87

3.4. Semiconducting Properties of Passive Films

As shown in Figure 5a, all MGs exhibit superior passivation behaviors in the potential range of 0.2–0.8 V_{SCE}. These MGs were polarized at 0.5 V_{SCE} for 30 min to obtain passive oxide films. The current density (i)–time (t) responses in Figure 7 present that i begins to drop sharply and eventually reaches a steady-state with the increase in t, suggesting the formation of passive films on the surfaces of MGs [48]. Endowed with the minimum i at the steady-state, A1 MG exhibits its superior corrosion resistance to the others, which is highly consistent with the potentiodynamic polarization and EIS results.

The corrosion resistance of metallic glasses is highly related to their passive film characteristics, such as the semiconducting property, chemical composition, and thickness. Given the imperfection of passive oxide films from crystallographic aspects, these films are generally identified as an n-type semiconductor for donor defects or a p-type semiconductor for acceptor defects [49]. The semiconducting properties of passive films are evaluated by the Mott–Schottky approaches, which represent the measured electrode capacitance as a function of the electrode potential. Generally, the electrode capacitance C_f is expressed as follows:

$$C_f^{-2} = C_{SC}^{-2} + C_H^{-2} + 2C_{SC}^{-1}C_H^{-1} \tag{1}$$

where C_{SC} and C_H stand for the capacitance of the space charge layer and Helmholtz layer, respectively. The availability of Mott–Schottky analysis hinges on the assumption that C_{SC} is much smaller than C_H. Under the test frequency of 10^3 Hz, the contribution of $2C_{SC}^{-1}C_H^{-1}$ and C_H^{-2} in Equation (1) is negligible; thus, the measured C_f equals to C_{SC}. For n-type semiconductors, C_{SC} is expressed in Equation (2) [50]:

$$C_{SC}^{-2} = \frac{2}{\varepsilon_0 \varepsilon_r N_D e}\left(E - E_{FB} - \frac{kT}{e}\right) \tag{2}$$

where ε_0 is the vacuum permittivity; ε_r is the dielectric constant of the passive film ($\varepsilon_r = 15.6$ [51]); e is the electron charge; E is the applied potential; E_{FB} is the flat band potential; k is the Boltzmann constant; T is the temperature in Kelvin; and N_D is the donor density, which is determined in Equation (3):

$$N_D = \frac{2}{\varepsilon_0 \varepsilon_r e}\left(\frac{dC^{-2}}{dE}\right)^{-1} \tag{3}$$
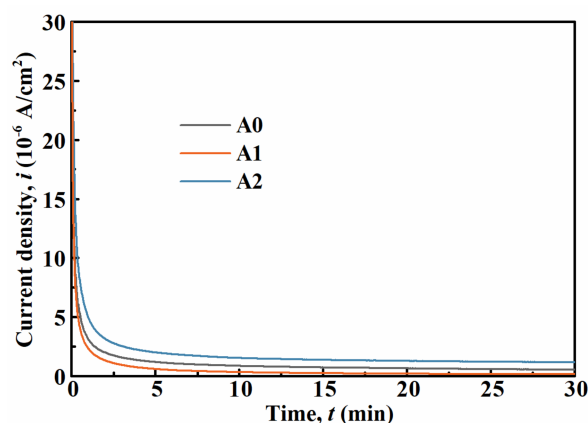

Figure 7. Potentiostatic polarization curves of MGs.

Mott–Schottky responses of the passive films formed on MGs are shown in Figure 8a. All three curves exhibit similar shapes with positive linear regions in the potential range of 0.4–0.7 V_{SCE}, illustrating that the passive films represent the n-type semiconductor and comprise the massive donor defects in this potential range [52]. As shown in Figure 8b, the calculated N_D values of passive films formed on the A0, A1, and A2 samples are approximately 4.40×10^{19}, 2.99×10^{19}, and 9.20×10^{19} cm^{-3}, respectively. Lower N_D indicates lower conductivity and better protective characteristics for passive films [53]. Thus, by reviewing the aforementioned N_D values, the passive film formed on A1 MG is relatively protective, whilst that formed on A2 MG is defective.
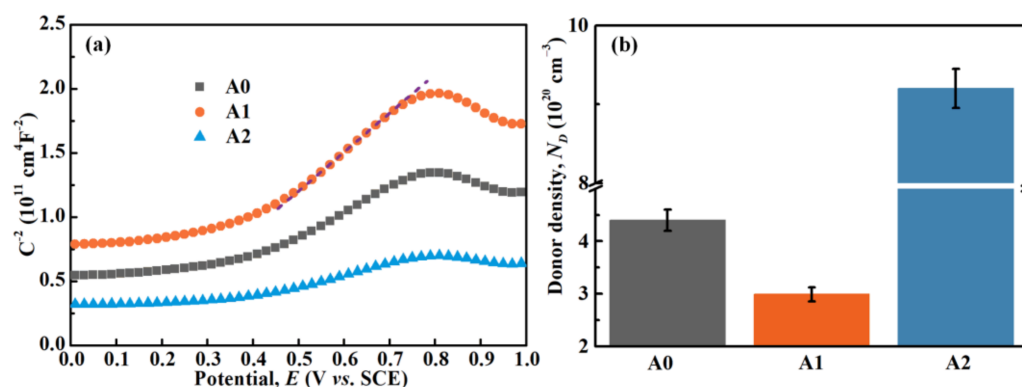

Figure 8. (**a**) Mott–Schottky plots and (**b**) the calculated N_D of the passive films that formed on MGs.

3.5. XPS Depth Profiling Analysis

XPS on analyzing the passive films of MGs (Figure 9) indicates the presence of Fe, Cr, Mo, W, Y, and O elements. The C element was excluded because it was considered as a contaminant during the measurement. The relative atomic concentrations of each element in passive films, calculated from the integrity of the peak area, are given in Figure 10. Apparently, the cationic Fe, Cr, Mo, W, and Y elements and the anionic O element in the passive films are diffused from the metal matrix and the electrolyte side, respectively. Among the three samples, the Cr concentration of the passive film surface that formed on A0, A1, and A2 samples is approximately 11.1 at %, 11.8 at %, and 10.3 at %, which is in a trend of A1 > A0 > A2. The surface enrichment of the Cr element could accelerate the formation of a passive film with greater resistance to the attack of Cl^- ions in acid media [54]. Therefore, a better corrosion-resistant performance can be expected for the A1 sample. Interestingly, the thicknesses of the passive films, which was considered as the thickness of oxide layers where the oxygen content is approximately half that of the initial surface [51,55], have the same trend as the concentration of surface Cr for the three samples. The calculated thicknesses, marked in a dashed line, are approximately 3.17, 3.33, and 2.99 nm for A0, A1, and A2 MGs, respectively. This result demonstrates that annealing MG at $0.7T_g$ thickens the passive film and improves its protectiveness. Instead, annealing MG at $T_g + 10$ K has an opposite effect on the passive film.
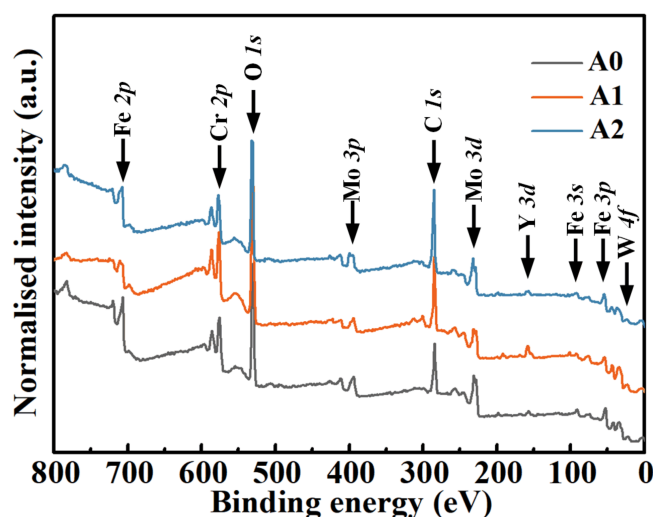

Figure 9. XPS survey spectra of the passive films without sputtering that formed on MGs.
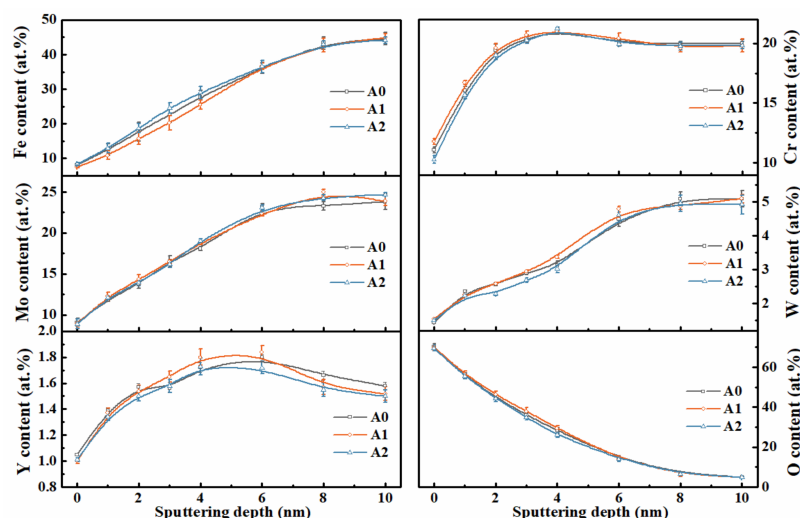

Figure 10. Depth profiles of elemental concentrations of the passive films that formed on the initial and annealed MGs.

Combined with the Mott–Schottky and XPS results, these passive film characteristics effectively explain the electrochemical behaviors of MGs in Figure 5. With a decreased N_D, higher concentration of surface Cr, and increased passive film thickness, a better passivity and excellent corrosion resistance are illustrated, suggesting a trend of A1 > A0 > A2 for Fe-based MGs. Therefore, the MGs annealed at different temperatures across the T_g region may give a distinct response to its corrosion resistance led by the multi-effects on the formation of a stable and protective passive film.

3.6. Effect of Annealing Temperature on the Structural Heterogeneity of MGs

According to the PEL theory, annealing MGs at different temperatures can readily obtain glassy structures with various energetic states. As shown in Figure 1b, the ΔH_{rel} value in DSC thermograms decreases from $\approx$7.51 to $\approx$6.71 J/g for MG annealed at 0.7 T_g, which could be explained by the active local atomic motions rather than the global atomic motion. The local atomic rearrangement through short-range diffusion or cooperative atomic motion is triggered by the release of the excess enthalpy [56]. As a consequence, the free volume in the amorphous structure reduces, and the atoms pack more compactly for A1 MG [57–59]. This structural change may lead to the loss of active sites that respond to the external corrosion attack.

On the increasing temperature, the thermal vibration energy becomes larger than the energy barrier, and it can lead to thermal activations for atom rearrangement in MGs [60]. When the annealing temperature reaches T_g, the large size atomic diffusion notably promotes the atomic transport [61]. Some fast degrees of freedom frozen in the deep glassy state are reactivated. The enlarged first coordination shell indicates that the atomic packing in the nearest neighbors becomes looser and there is more free space to move in three dimensions. Hence, annealing MG at Tg + 10 K generates larger-sized MRO clusters, as shown in the TEM images. This process is related to an incipient crystallization as the thermal activation coincides with a marked increased medium-range ordering and a dilatation of the third shell [8]. This dilatation is also evidenced by the increased r_3 and r_4 peaks in PDF analysis.

3.7. Correlation Between the Structural Heterogeneity and Corrosion Performance of MGs

Mainly, the structural heterogeneity, considering the atom packing density and the presence of a crystal-like cluster, is strongly correlated with the performance of electrochemical corrosion and the characteristics of the formed passive film. For the A1 sample, annealing MG at 0.7 T_g leads to a reduction in free volume, which in turn yields a more compact structure between atoms and decreases the chemical potential. In this case, the atoms are supposed to lie on a lower energy joint in the crystal field that makes them become less electrochemically active and cannot be easily removed during dissolution [62]. Moreover, the atomic densification favors the compactness and protectiveness of the formed surface passive films. As a result, the formation of a stable and protective passive film is favorable, and it can effectively prevent the absorption/penetration of Cl$^-$ ions and other chemical exchanges on the surface of MGs, leading to a superior corrosion resistance property [22]. However, annealing MG above T_g generates some larger-sized MRO clusters. As shown in Figure 3c,d, such nanoscale crystal-like clusters were embedded in the amorphous matrix. In addition, the structural heterogeneity induces micro-electrochemical cells around the boundary of the crystal-like clusters and the amorphous matrix [63]. These cells in passive films are expected to be terminal points for the permeation of Cl$^-$ ions and act as preferential sites for pitting initiation and propagation [64,65]. From a structural viewpoint, the corrosion generally originates from a loose-packing structure and the presence of defects. The loose atomic packing, as shown by PDF analysis, leaves more free space for the absorption/penetration of Cl$^-$ ions. Thereby, both these distinct microstructures accelerate the corrosion process of MG.

4. Conclusions

In conclusion, the effect of annealing on the structural heterogeneity of Fe-Cr-Mo-W-C-B-Y MGs and its correlation with the electrochemical behavior and passive film characteristic were investigated. Annealing MG at 0.7 T_g for 30 min led to the reduced free volume and the shrinkage of the first coordination shell in the local atomic structure, which could improve the passivity and corrosion resistance, indicating from the decreased i_{pass}, elevated E_{pit}, and increased R_c. The reason suggested was that such microstructures favored the formation of more compact and protective passive films. In contrast, MG annealed at $T_g + 10$ K for 30 min exhibited a distinct microstructure, considering the enlarged first coordination shell and the presence of nanoscale crystal-like clusters, which deteriorated the protectiveness of the passive film and thereby decreased the corrosion resistance. Departing from the different annealing temperatures across the T_g point for Fe-based MGs, this study successfully determined the effect of annealing on the structural heterogeneity and established its correlation with corrosion performance of Fe-based MGs. The importance of structural heterogeneity is giving new insight into understanding the corrosion mechanism of MGs.

Institutional Review Board Statement: Not applicable.

Informed Consent Statement: Not applicable.

Data Availability Statement: The raw/processed data required to reproduce these findings cannot be shared at this time as the data also forms part of an ongoing study.

Conflicts of Interest: The authors declare no conflict of interest.

References

1. Rezaei-Shahreza, P.; Seifoddini, A.; Hasani, S.; Jaafari, Z.; Sliwa, A.; Nabialek, M. Isokinetic Analysis of Fe(41)Co(7)Cr(15)Mo(14) Y(2)C(15)B(6)Bulk Metallic Glass: Effect of Minor Copper Addition. *Materials* **2020**, *13*, 3704. [CrossRef]
2. Sagasti, A.; Palomares, V.; Porro, J.M.; Orúe, I.; Sánchez-Ilárduya, M.B.; Lopes, A.C.; Gutiérrez, J. Magnetic, Magnetoelastic and Corrosion Resistant Properties of (Fe–Ni)-Based Metallic Glasses for Structural Health Monitoring Applications. *Materials* **2019**, *13*, 57. [CrossRef]
3. Hirata, A.; Guan, P.; Fujita, T.; Hirotsu, Y.; Inoue, A.; Yavari, A.R.; Sakurai, T.; Chen, M. Direct observation of local atomic order in a metallic glass. *Nat. Mater.* **2010**, *10*, 28–33. [CrossRef]
4. Zhu, F.; Hirata, A.; Liu, P.; Song, S.; Tian, Y.; Han, J.; Fujita, T.; Chen, M. Correlation between Local Structure Order and Spatial Heterogeneity in a Metallic Glass. *Phys. Rev. Lett.* **2017**, *119*, 215501. [CrossRef]
5. Wagner, H.; Bedorf, D.; Kuechemann, S.; Schwabe, M.; Zhang, B.; Arnold, W.; Samwer, K. Local elastic properties of a metallic glass. *Nat. Mater.* **2011**, *10*, 439–442. [CrossRef] [PubMed]
6. Liu, Y.H.; Wang, D.; Nakajima, K.; Zhang, W.; Hirata, A.; Nishi, T.; Inoue, A.; Chen, M.W. Characterization of Nanoscale Mechanical Heterogeneity in a Metallic Glass by Dynamic Force Microscopy. *Phys. Rev. Lett.* **2011**, *106*, 125504. [CrossRef] [PubMed]
7. Lan, S.; Ren, Y.; Wei, X.Y.; Wang, B.; Gilbert, E.P.; Shibayama, T.; Watanabe, S.; Ohnuma, M.; Wang, X.-L. Hidden amorphous phase and reentrant supercooled liquid in Pd-Ni-P metallic glasses. *Nat. Commun.* **2017**, *8*, 14679. [CrossRef] [PubMed]
8. Giordano, V.M.; Ruta, B. Unveiling the structural arrangements responsible for the atomic dynamics in metallic glasses during physical aging. *Nat. Commun.* **2016**, *7*, 10344. [CrossRef] [PubMed]
9. Șopu, D.; Yuan, X.; Moitzi, F.; Stoica, M.; Eckert, J. Structure⁻Property Relationships in Shape Memory Metallic Glass Composites. *Materials* **2019**, *12*, 1419. [CrossRef]

10. Liu, Y.H.; Wang, G.; Wang, R.J.; Zhao, D.Q.; Pan, M.X.; Wang, W.H. Super Plastic Bulk Metallic Glasses at Room Temperature. *Science* **2007**, *315*, 1385–1388. [CrossRef]

11. Sarac, B.; Ivanov, Y.P.; Chuvilin, A.; Schöberl, T.; Stoica, M.; Zhang, Z.; Eckert, J. Origin of large plasticity and multiscale effects in iron-based metallic glasses. *Nat. Commun.* **2018**, *9*, 1333. [CrossRef]

12. Bednarcik, J.; Michalik, S.; Kolesar, V.; Rütt, U.; Franz, H. In situ XRD studies of nanocrystallization of Fe-based metallic glass: A comparative study by reciprocal and direct space methods. *Phys. Chem. Chem. Phys.* **2013**, *15*, 8470. [CrossRef]

13. Ouyang, S.; Song, L.J.; Liu, Y.H.; Huo, J.T.; Wang, J.Q.; Xu, W.; Li, J.L.; Wang, C.T.; Wang, X.M.; Li, R.W. Correlation between the viscoelastic heterogeneity and the domain wall motion of Fe-based metallic glass. *Phys. Rev. Mater.* **2018**, *2*, 063601. [CrossRef]

14. Wang, X.; Pan, Y.; Zhu, Z.; Wu, J. Efficient degradation of rhodamine B using Fe-based metallic glass catalyst by Fenton-like process. *Chemosphere* **2014**, *117*, 638–643. [CrossRef] [PubMed]

15. Li, R.; Liu, X.; Wang, H.; Zhou, D.; Wu, Y.; Lu, Z. Formation mechanism and characterization of nanoporous silver with tunable porosity and promising capacitive performance by chemical dealloying of glassy precursor. *Acta Mater.* **2016**, *105*, 367–377. [CrossRef]

16. Hu, Y.C.; Wang, Y.Z.; Su, R.; Cao, C.R.; Lin, W.Z.; Sun, C.W.; Yang, Y.; Guan, P.F.; Ding, D.W.; Wang, Z.L.; et al. A Highly Efficient and Self-Stabilizing Metallic-Glass Catalyst for Electrochemical Hydrogen Generation. *Adv. Mater.* **2016**, *28*, 10293–10297. [CrossRef] [PubMed]

17. Jiang, W.H.; Jiang, F.; Green, B.A.; Liu, F.X.; Liaw, P.K.; Choo, H.; Qiu, K.Q. Electrochemical corrosion behavior of a Zr-based bulk-metallic glass. *Appl. Phys. Lett.* **2007**, *91*, 041904. [CrossRef]

18. Zhang, L.; Zhang, S.; Ma, A.; Hu, H.; Zheng, Y.; Yang, B.; Wang, J. Thermally induced structure evolution on the corrosion behavior of Al-Ni-Y amorphous alloys. *Corros. Sci.* **2018**, *144*, 172–183. [CrossRef]

19. Tailleart, N.; Huang, R.; Aburada, T.; Horton, D.; Scully, J. Effect of thermally induced relaxation on passivity and corrosion of an amorphous Al–Co–Ce alloy. *Corros. Sci.* **2012**, *59*, 238–248. [CrossRef]

20. Duarte, M.J.; Klemm, J.; Klemm, S.O.; Mayrhofer, K.J.J.; Stratmann, M.; Borodin, S.; Romero, A.H.; Madinehei, M.; Crespo, D.; Serrano, J.; et al. Element-Resolved Corrosion Analysis of Stainless-Type Glass-Forming Steels. *Science* **2013**, *341*, 372–376. [CrossRef]

21. Jindal, R.; Raja, V.; Gibson, M.; Styles, M.; Bastow, T.; Hutchinson, C. Effect of annealing below the crystallization temperature on the corrosion behavior of Al–Ni–Y metallic glasses. *Corros. Sci.* **2014**, *84*, 54–65. [CrossRef]

22. Tang, J.; Yu, L.; Qiao, J.; Wang, Y.; Wang, H.; Duan, M.; Chamas, M. Effect of atomic mobility on the electrochemical properties of a Zr58Nb3Cu16Ni13Al10 bulk metallic glass. *Electrochim. Acta* **2018**, *267*, 222–233. [CrossRef]

23. Filik, J.; Ashton, A.W.; Chang PC, Y.; Chater, P.A.; Day, S.J.; Drakopoulos, M.; Gerring, M.W.; Hart, M.L.; Magdysyuk, O.V.; Michalik, S.; et al. Processing two-dimensional X-ray diffraction and small-angle scattering data in *DAWN 2. J. Appl. Crystallogr.* **2017**, *50*, 959–966. [CrossRef]

24. Basham, M.; Filik, J.; Wharmby, M.T.; Chang, P.C.; El Kassaby, B.; Gerring, M.; Aishima, J.; Levik, K.; Pulford, B.C.A.; Sikharulidze, I.; et al. Data Analysis WorkbeNch (DAWN). *J. Synchrotron Radiat.* **2015**, *22*, 853–858. [CrossRef] [PubMed]

25. Qiu, X.; Thompson, J.W.; Billinge, S.J.L. PDFgetX2: A GUI-driven program to obtain the pair distribution function from X-ray powder diffraction data. *J. Appl. Crystallogr.* **2004**, *37*, 678. [CrossRef]

26. Liang, D.; Ma, J.; Cai, Y.; Liu, X.; Xie, S.; Wei, X.; Xu, G.; Shen, J. Characterization and elevated-temperature tribological performance of AC–HVAF-sprayed Fe-based amorphous coating. *Surf. Coat. Technol.* **2020**, *387*, 125535. [CrossRef]

27. Lou, Y.; Xv, S.; Liu, Z.; Ma, J. Rejuvenation of Zr-Based Bulk Metallic Glasses by Ultrasonic Vibration-Assisted Elastic Deformation. *Materials* **2020**, *13*, 4397. [CrossRef]

28. Murali, P.; Ramamurty, U. Embrittlement of a bulk metallic glass due to sub-Tg annealing. *Acta Mater.* **2005**, *53*, 1467–1478. [CrossRef]

29. Shin, S.S.; Kim, H.K.; Lee, J.C.; Park, I.M. Effect of Sub-Tg Annealing on the Corrosion Resistance of the Cu–Zr Amorphous Alloys. *Acta Metall. Sin. (Engl. Lett.)* **2017**, *31*, 273–280. [CrossRef]

30. Wang, X.; Gong, P.; Deng, L.; Jin, J.; Wang, S.; Li, F. Sub-Tg annealing effect on the kinetics of glass transition and crystallization for a Ti-Zr-Be-Fe bulk metallic glass. *J. Non-Cryst. Solids* **2017**, *473*, 132–140. [CrossRef]

31. An, Y.; Hou, G.; Chen, J.; Zhao, X.; Liu, G.; Zhou, H.; Chen, J. Microstructure and tribological properties of iron-based metallic glass coatings prepared by atmospheric plasma spraying. *Vacuum* **2014**, *107*, 132–140. [CrossRef]

32. Stillinger, F.H. A Topographic View of Supercooled Liquids and Glass Formation. *Science* **1995**, *267*, 1935–1939. [CrossRef] [PubMed]

33. Sastry, S.; DeBenedetti, P.G.; Stillinger, F.H. Signatures of distinct dynamical regimes in the energy landscape of a glass-forming liquid. *Nat. Cell Biol.* **1998**, *393*, 554–557. [CrossRef]

34. DeBenedetti, P.G.; Stillinger, F.H. Supercooled liquids and the glass transition. *Nat. Cell Biol.* **2001**, *410*, 259–267. [CrossRef] [PubMed]

35. Evenson, Z.; Koschine, T.; Wei, S.; Gross, O.; Bednarcik, J.; Gallino, I.; Kruzic, J.J.; Rätzke, K.; Faupel, F.; Busch, R. The effect of low-temperature structural relaxation on free volume and chemical short-range ordering in a Au49Cu26.9Si16.3Ag5.5Pd2.3 bulk metallic glass. *Scr. Mater.* **2015**, *103*, 14–17. [CrossRef]

36. Lelito, J. Crystallization Kinetics Analysis of the Amorphouse Mg(72)Zn(24)Ca(4)Alloy at the Isothermal Annealing Temperature of 507 K. *Materials* **2020**, *13*, 2815. [CrossRef] [PubMed]

37. Cheng, Y.; Ma, E. Atomic-level structure and structure–property relationship in metallic glasses. *Prog. Mater. Sci.* **2011**, *56*, 379–473. [CrossRef]

38. Pan, S.P.; Qin, J.Y.; Wang, W.M.; Gu, T.K. Origin of splitting of the second peak in the pair-distribution function for metallic glasses. *Phys. Rev. B* **2011**, *84*, 092201. [CrossRef]

39. Jiang, H.-R.; Bochtler, B.; Frey, M.; Liu, Q.; Wei, X.-S.; Min, Y.; Riegler, S.S.; Liang, D.-D.; Busch, R.; Shen, J. Equilibrium viscosity and structural change in the Cu47.5Zr45.1Al7.4 bulk glass-forming liquid. *Acta Mater.* **2020**, *184*, 69–78. [CrossRef]

40. Yang, Y.; Zeng, J.; Volland, A.; Blandin, J.; Gravier, S.; Liu, C. Fractal growth of the dense-packing phase in annealed metallic glass imaged by high-resolution atomic force microscopy. *Acta Mater.* **2012**, *60*, 5260–5272. [CrossRef]

41. Oliver, W.; Pharr, G. An improved technique for determining hardness and elastic modulus using load and displacement sensing indentation experiments. *J. Mater. Res.* **1992**, *7*, 1564–1583. [CrossRef]

42. Liu, X.; Li, F.; Yang, Y. "Softness" as the structural origin of plasticity in disordered solids: A quantitative insight from machine learning. *Sci. China Mater.* **2018**, *62*, 154–160. [CrossRef]

43. Stolpe, M.; Kruzic, J.J.; Busch, R. Evolution of shear bands, free volume and hardness during cold rolling of a Zr-based bulk metallic glass. *Acta Mater.* **2014**, *64*, 231–240. [CrossRef]

44. Louzguineluzgin, D.V.; Bazlov, A.; Ketov, S.; Greer, A.; Inoue, A. Crystal growth limitation as a critical factor for formation of Fe-based bulk metallic glasses. *Acta Mater.* **2015**, *82*, 396–402. [CrossRef]

45. Louzguine-Luzgin, D.; Bazlov, A.; Ketov, S.; Inoue, A. Crystallization behavior of Fe- and Co-based bulk metallic glasses and their glass-forming ability. *Mater. Chem. Phys.* **2015**, *162*, 197–206. [CrossRef]

46. Khan, M.M.; Shabib, I.; Haider, W. A combinatorially developed Zr-Ti-Fe-Al metallic glass with outstanding corrosion resistance for implantable medical devices. *Scr. Mater.* **2019**, *162*, 223–229. [CrossRef]

47. Kocijan, A.; Merl, D.K.; Jenko, M. The corrosion behaviour of austenitic and duplex stainless steels in artificial saliva with the addition of fluoride. *Corros. Sci.* **2011**, *53*, 776–783. [CrossRef]

48. Qiao, Y.; Zheng, Y.; Ke, W.; Okafor, P. Electrochemical behaviour of high nitrogen stainless steel in acidic solutions. *Corros. Sci.* **2009**, *51*, 979–986. [CrossRef]

49. Liang, D.-D.; Wei, X.-S.; Chang, C.-T.; Li, J.-W.; Wang, Y.; Wang, X.-M.; Shen, J. Effects of W Addition on the Electrochemical Behaviour and Passive Film Properties of Fe-Based Amorphous Alloys in Acetic Acid Solution. *Acta Met. Sin. (English Lett.)* **2018**, *31*, 1098–1108. [CrossRef]

50. Wang, Z.; Ma, Y.; Zhang, J.; Hou, W.; Chang, X.; Wang, J. Influence of yttrium as a minority alloying element on the corrosion behavior in Fe-based bulk metallic glasses. *Electrochim. Acta* **2008**, *54*, 261–269. [CrossRef]

51. Liang, D.; Wei, X.; Wang, Y.; Jiang, H.; Shen, J. Electrochemical behaviors and passive film properties of Fe-based bulk metallic glass in Cl−-containing acetic acid solutions under high temperature. *J. Alloys Compd.* **2018**, *766*, 964–972. [CrossRef]

52. Ningshen, S.; Mudali, U.K.; Mittal, V.; Khatak, H. Semiconducting and passive film properties of nitrogen-containing type 316LN stainless steels. *Corros. Sci.* **2007**, *49*, 481–496. [CrossRef]

53. Fernández-Domene, R.M.; Blasco-Tamarit, E.; García-García, D.M.; Garcia-Anton, J. Passivity Breakdown of Titanium in LiBr Solutions. *J. Electrochem. Soc.* **2013**, *161*, C25–C35. [CrossRef]

54. Xu, D.; Zhou, B.; Wang, Q.; Zhou, J.; Yang, W.; Yuan, C.; Xue, L.; Fan, X.; Ma, L.; Shen, B. Effects of Cr addition on thermal stability, soft magnetic properties and corrosion resistance of FeSiB amorphous alloys. *Corros. Sci.* **2018**, *138*, 20–27. [CrossRef]

55. Man, C.; Dong, C.; Cui, Z.; Xiao, K.; Yu, Q.; Li, X. A comparative study of primary and secondary passive films formed on AM355 stainless steel in 0.1 M NaOH. *Appl. Surf. Sci.* **2018**, *427*, 763–773. [CrossRef]

56. Zhu, F.; Nguyen, H.K.; Song, S.X.; Aji, D.P.B.; Hirata, A.; Wang, H.; Nakajima, K.; Chen, M.W. Intrinsic correlation between β-relaxation and spatial heterogeneity in a metallic glass. *Nat. Commun.* **2016**, *7*, 11516. [CrossRef]

57. Gu, B.; Liu, F. Characterization of structural inhomogeneity in Al88Ce8Co4 metallic glass. *Acta Mater.* **2016**, *112*, 94–104. [CrossRef]

58. Huang, Y.; Fan, H.; Zhou, X.; Xue, P.; Ning, Z.; Daisenberger, D.; Sun, J.; Shen, J. Structure and mechanical property modification of a Ti-based metallic glass by ion irradiation. *Scr. Mater.* **2015**, *103*, 41–44. [CrossRef]

59. Evertz, S.; Schneider, J.M. Effect of the Free Volume on the Electronic Structure of Cu70Zr30 Metallic Glasses. *Materials* **2020**, *13*, 4911.

60. Liu, W.; Ruan, H.; Zhang, L. Atomic rearrangements in metallic glass: Their nucleation and self-organization. *Acta Mater.* **2013**, *61*, 6050–6060. [CrossRef]

61. Wang, Y.-J.; Du, J.-P.; Shinzato, S.; Dai, L.-H.; Ogata, S. A free energy landscape perspective on the nature of collective diffusion in amorphous solids. *Acta Mater.* **2018**, *157*, 165–173. [CrossRef]

62. González, S.; Pellicer, E.; Suriñach, S.; Baró, M.D.; Sort, J. Mechanical and corrosion behaviour of as-cast and annealed Zr60Cu20Al10Fe5Ti5 bulk metallic glass. *Intermetallics* **2012**, *28*, 149–155. [CrossRef]

63. Zhao, G.; Zou, Y.; Zhang, H.; Zou, Z. Correlation between corrosion resistance and the local atomic structure of electroless, annealed Ni–P amorphous alloys. *Mater. Lett.* **2014**, *132*, 221–223. [CrossRef]

64. Zhang, B.; Wang, J.; Wu, B.; Guo, X.W.; Wang, Y.J.; Chen, D.; Zhang, Y.C.; Du, K.; Oguzie, E.E.; Ma, X.L. Unmasking chloride attack on the passive film of metals. *Nat. Commun.* **2018**, *9*, 1–9. [CrossRef]

65. Gebert, A.; Gostin, P.; Uhlemann, M.; Eckert, J.; Schultz, L. Interactions between mechanically generated defects and corrosion phenomena of Zr-based bulk metallic glasses. *Acta Mater.* **2012**, *60*, 2300–2309. [CrossRef]